Zitierweise: *Angew. Chem. Int. Ed.* **2025**, e202502005
doi.org/10.1002/anie.202502005

Zn–I$_2$ Batteries **Hot Paper**

SiO$_2$ Nanoparticles-Induced Antifreezing Hydrogel Electrolyte Enables Zn–I$_2$ Batteries with Complete and Reversible Four-Electron-Transfer Mechanisms at Low Temperatures

Minghui Chen$^+$, Guanhong Chen$^+$, Chenxi Sun, Xinyu Li, Minghao Zhang, Haiming Hua, Jinbao Zhao, and Yang Yang**

Abstract: Four-electron-transfer aqueous zinc–iodine batteries hold significant promise for large-scale energy storage due to their high specific capacities. However, achieving four-electron-transfer mechanisms under sub-zero temperatures remains challenging due to freezing point limitations of conventional aqueous electrolytes and sluggish reaction kinetics. Herein, an antifreezing hydrogel electrolyte (HC-SiO$_2$) is developed through the spontaneous gelation of a high-concentration electrolyte (1 m Zn(OAc)$_2$ + 21 m LiCl, HC) with SiO$_2$ nanoparticles, enabling low-temperature operation of quasi-solid-state Zn–I$_2$ batteries with complete and reversible four-electron-transfer processes. Abundant interactions between dispersed SiO$_2$ nanoparticles and cations enlarge ion-pair distances, reducing close ion-pair formation and lowering the freezing temperature (−60.7 °C). Furthermore, the quasi-solid-state hydrogel electrolyte combines advantages of reduced water activity and disrupted hydrogen-bond networks, effectively suppressing I$^+$ hydrolysis while inhibiting ice nucleation. Additionally, the utilization of low-concentration Zn(OAc)$_2$ combined with high-concentration LiCl increases availability of free Cl$^-$ by mitigating strong ionic interaction in conventional ZnCl$_2$-based concentrated electrolytes, thereby enhancing reaction kinetics of the I$_2$/I$^+$ conversion. Benefiting from synergistic manipulation of ionic interaction, water activity, and Cl$^-$ activity, the HC-SiO$_2$ hydrogel achieves a high capacity of 490.9 mAh g^{-1} and durable lifespan exceeding 11,000 cycles at −20 °C. These findings offer valuable insights for advancing practical low-temperature Zn–I$_2$ batteries.

Introduction

Motivated by the pursuit of safer and more efficient battery technologies in large-scale electrical energy storage,[1,2] aqueous Zn metal batteries have attracted significant research attention due to their inherent high safety and low cost.[3,4] Among these, aqueous zinc–iodine (Zn–I$_2$) batteries stand out for their distinct advantages, including abundant availability of zinc in the Earth's crust and iodine in seawater, as well as their environmental friendliness and recyclability.[5,6] Nonetheless, substantial improvements in energy density, cycling stability, and especially cold-weather performance are still required to meet demands of rapidly expanding applications across diverse geographical regions.[7,8] Fortunately, the theoretical capacity of iodine cathode can be significantly enhanced from 221 mAh g^{-1} (based on the I$_2$/I$^-$ conversion) to 442 mAh g^{-1} by activating the additional I$^+$/I$_2$ redox reaction.[9] Qiao et al. predicted that a considerable cell-level energy density of 128.8 Wh kg^{-1} could be achieved in a hypothetical 12 Ah pouch battery leveraging this four-electron-transfer mechanism.[8] However, the I$^+$ hydrolysis caused by nucleophilic attacks from water molecules, as well as the sluggish reaction kinetics of I$^+$/I$_2$ redox couple, impede both the reversibility and low-temperature capacity performance of aqueous Zn–I$_2$ batteries.[10,11]

To effectively stabilize I$^+$ species in aqueous environments, various strategies have been explored, including host modification,[9,12–14] electrocatalyst implementation,[15,16] and electrolyte design.[17–24] Among these, the development of highly concentrated ZnCl$_2$-based electrolytes, which exhibit exceptional solubility (up to 38 m), has emerged as a representative strategy. These electrolytes facilitate the formation of I$^+$Cl$^-$ complexes and mitigate water-induced hydrolysis due to their low free water content.[17] Moreover, concentrated electrolytes also lower freezing temperatures compared to conventional diluted electrolytes by disrupting the hydrogen-bond (H-bond) network in water.[25–27] However, the ion association structures in such systems (Figure 1a) becomes increasingly sensitive to temperature drops, leading to enhanced ionic binding and precipitation at low temperatures (Figure 1b), which limits further reduction in freezing points.[26,28,29] To address these limitations, He et al. reduced the ZnCl$_2$ concentration to 15 m and introduced functional tetraethylammonium cations (TEA$^+$), achieving a capacity of 306.7 mAh g^{-1} at −20 °C.[24] Similarly, Liang et al. incorporated polyethylene glycol (PEG) as a cosolvent in 2 m

---

[*] M. Chen$^+$, G. Chen$^+$, C. Sun, M. Zhang, H. Hua, J. Zhao, Y. Yang
State Key Lab of Physical Chemistry of Solid Surfaces, State-Province Joint Engineering Laboratory of Power Source Technology for New Energy Vehicle, College of Chemistry and Chemical Engineering, Xiamen University, Xiamen 361005, P.R. China
E-mail: jbzhao@xmu.edu.cn
yangyang419@xmu.edu.cn

X. Li
College of Energy, Xiamen University, Xiamen 361005, P.R. China

[+] These authors contributed equally to this work.

Additional supporting information can be found online in the Supporting Information section

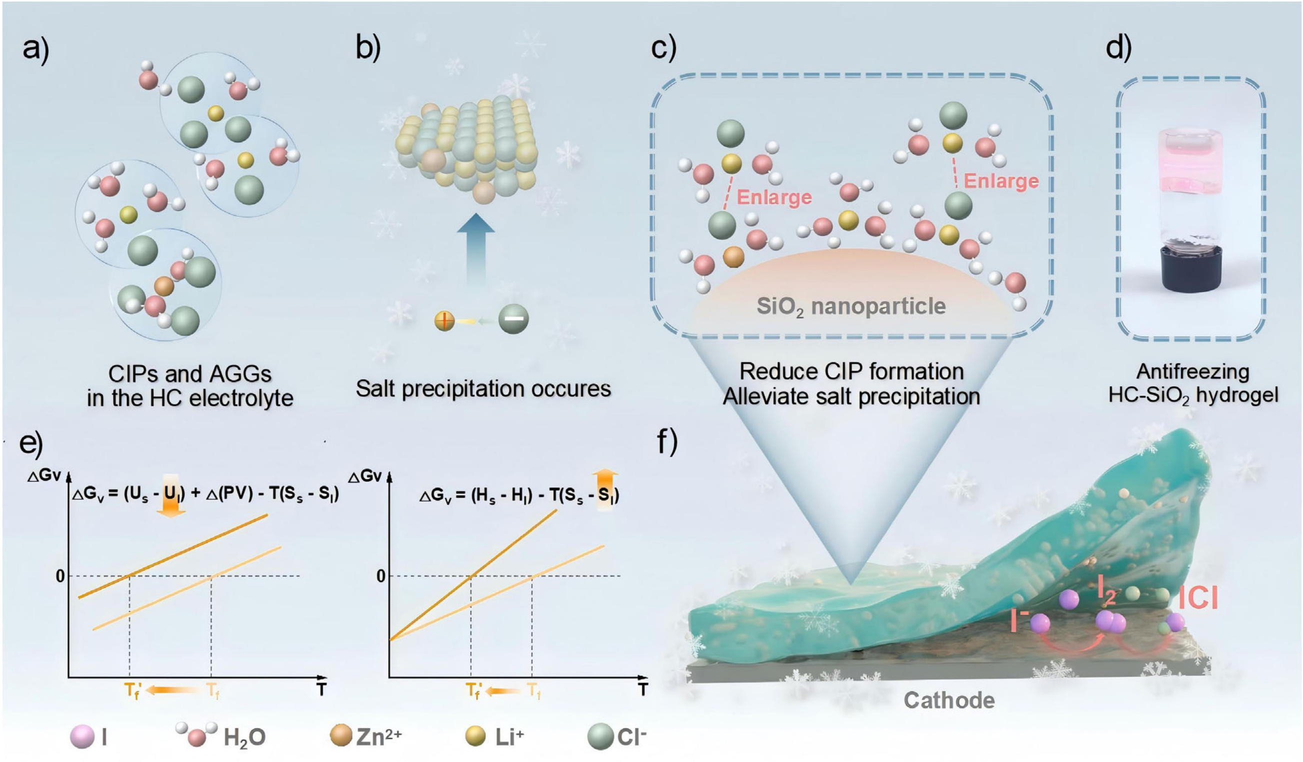

Figure 1. a–c) Schematic illustrations of a) CIPs and AGGs in the HC electrolyte, b) their salt precipitation occurring at low temperatures, and c) enlarged distances between anions and cations through the interactions of SiO_2 surface with water and cations. d) Photograph of the HC-SiO_2 hydrogel exhibiting Tyndall scattering. e) Relationship among Gibbs free energy (G), enthalpy (H), internal energy (U), entropy (S), and the freezing point (T_f). The l and s denote liquid and solid state of the system, respectively. f) Schematic illustration of the HC-SiO_2 hydrogel enabling the $I^+/I_2/I^-$ conversion of iodine cathode at low temperatures.

$ZnCl_2$ aqueous solution, enhancing the capacity to 329.8 mAh g^{-1} at –25 °C.[21] Despite these advancements, achieving the complete four-electron-transfer reaction pathway with a high capacity approaching the theoretical value of 442 mAh g^{-1} at subzero temperatures remains a significant challenge.

From a thermodynamic perspective, the freezing temperature of an electrolyte is determined by the Gibbs free energy change during solidification (Supporting Information). In a concentrated electrolyte, freezing is primarily influenced by an increase in internal energy (U_l) and a decrease in entropy (S_l), both of which are associated with the formation of close ion-pairs (CIPs) and aggregations (AGGs).[30,31] Therefore, suppressing CIP formation is a fundamental approach to delaying solidification. Although widely adopted strategies of reducing salt concentration reduce CIP formation and mitigate ionic interactions, they also diminish the ability to reduce water activity, potentially compromising cycling stability.[32] According to the Bjerrum's ion-pair formation theory ($\theta = \int_a^{r_{min}} P_r^i dr$, Supporting Information), the probability of ion-pair formation (θ) is also associated with the distance between oppositely charged ions. This inspires the development of novel suspension electrolyte systems that achieve ion-pair dissociation through the adsorption of charged ions onto dispersions.[33–36] In addition to improving the antifreezing property of the electrolyte, maintaining high Cl^- activity is also crucial for enabling complete I^+/I_2 redox conversion at low temperatures, as indicated by the reaction equilibrium ($I_2 + 2Cl^- \rightarrow 2ICl + 2e^-$).[17,37] However, in $ZnCl_2$ solutions, Cl^- ions predominantly associate with Zn^{2+} ions in the solvation sheath due to their strong interactions,[38] reducing the proportion of free Cl^- ions available for redox reactions.[25,39] Therefore, designing an ideal low-temperature electrolyte for high-capacity four-electron Zn–I_2 batteries necessitates balancing the ionic interaction, water activity, and the availability of free Cl^-.

In this work, we develop an antifreezing hydrogel electrolyte (HC-SiO_2) by dispersing SiO_2 nanoparticles (Figure S1) into a newly-designed high-concentration electrolyte (1 m $Zn(OAc)_2$ + 21 m LiCl, HC), enabling high-capacity quasi-solid-state Zn–I_2 batteries operating even at subzero temperatures. The HC electrolyte employs a design combining low-concentration $Zn(OAc)_2$ with high-concentration LiCl, thereby preventing the Zn^{2+}/Cl^- concentration dependence of conventional $ZnCl_2$ electrolytes, which effectively enhances Cl^- activity by leveraging the competition between Li^+–Cl^- associations while avoiding strong Zn^{2+}–Cl^- interactions. Unlike conventional hydrogels prepared using water-soluble polymers, abundant oxygen atoms on the surface of SiO_2 nanoparticles interact with water molecules and cations (Figure 1c) in the HC electrolyte, facilitating gelation formation (Figure 1d). Besides, these interactions enlarge ion-pair distances (Figure 1c), suppressing the formation of

CIPs and AGGs. Consequently, salt precipitation is alleviated, further lowering the freezing point thermodynamically by the reduced system energy and increased entropy (Figure 1e). Moreover, the quasi-solid-state hydrogel electrolyte also integrates the advantages of reduced water activity and disrupted H-bond network, effectively suppressing I^+ hydrolysis while inhibiting ice nucleation. Consequently, the HC-SiO_2 hydrogel achieves complete four-electron transfer (Figure 1f) and prolonged cycling life even at −20 °C, underscoring its practical potential for low-temperature applications.

Results and Discussion

Gelation Behaviour of SiO_2 Nanoparticles

To investigate the effect of SiO_2 nanoparticles on gelation, the SiO_2 content and salt concentration in the electrolytes were regulated for preliminary observations. As shown in Figures 2a and S2, when the mass percentage of SiO_2 reaches 6 wt%, the HC electrolyte or water transforms into immobile gel. Similarly, other electrolytes at various concentrations can remain in gel states upon the incorporation of 6 wt% SiO_2 (Figure 2b), indicating that the degree of gelation is primarily influenced by the SiO_2 content. Notably, reducing the LiCl concentration from 21 to 1 m causes a visible change in the gel electrolyte from transparent to opaque (Figure 2b), implying potential interactions between SiO_2 and ions. Furthermore, Fourier transform infrared (FT-IR) spectra of different electrolytes (Figures 2c and S3) reveal that the chemical environment on the SiO_2 surface is influenced by water and ions, as evidenced by shifts of Si—O bond peaks, particularly in concentrated electrolytes with 6 wt% SiO_2. Zeta potential measurements further support these findings. The SiO_2 in water exhibits a negative zeta potential (−2.93 mV), whereas transforming to positive values in the LiCl and $Zn(OAc)_2$ solution (Figure 2d)—even solutions with other cations (Figure S4)—indicating the cation-adsorptive nature of SiO_2 that is independent of cation type, due to negatively charged oxygen atoms exposed on the SiO_2 surface (Figure S1c).[40–42] Density functional theory (DFT) calculations further corroborate these results, showing negative binding energies for water or cations adsorption onto SiO_2 (Figures 2e and S5). The sufficient adsorption of cations homogenizes SiO_2 surface charge, enabling SiO_2 nanoparticles to be well-dispersed in solution through repulsive Coulomb force,[43] which contributes to forming a homogeneous and transparent electrolyte. Furthermore, introducing 6 wt% SiO_2 in the HC electrolyte can form a hydrogel with a recoverable "–SiO_2–water/ions–SiO_2–" interconnected network in which SiO_2 nanoparticles are bridged through interactions with water and ions, as revealed by the shear thinning behavior (Figure 2f and Table S1).[34] However, excessive SiO_2 content (e.g., 7 wt%) causes electrolyte turbidity (Figure S6a) due to insufficiently dispersed SiO_2 nanoparticles (Figure S6b,c). Consequently, SiO_2 dispersion regulated by cation adsorption is critical for maintaining electrolyte transparency and gel homogeneity.

Although gelation increases the viscosity of the HC electrolyte (Table S2), it does not negatively impact ionic conductivity at room temperature. Surprisingly, the gelation process further reduces the freezing point from −46.9 to −60.7 °C and enhances ionic conductivities below 0 °C (Figure 2g–h and Tables S3, S4). Remarkably, at −60 °C, the HC-SiO_2 hydrogel exhibits a significantly higher ionic conduction of 0.354 mS cm^{-1}. Simultaneously, the stability of the high-concentration electrolyte at low temperatures is improved, as revealed by increased activation energy (Figure 2i and Table S5). Besides, SiO_2 nanoparticles in the HC-SiO_2 hydrogel can be dispersed uniformly even at −40 °C, as evidenced by the Tyndall effect (Figure S7).

Investigation into the Freezing Point Depression

From the perspective of the water freezing process, the continuous H-bond network facilitates ice nucleation and the orderly solid-phase transition of water to ice below 0 °C.[44–46] Therefore, regulating the H-bond network within an aqueous electrolyte is essential for suppressing ice formation and lowering the freezing point.[26] As illustrated in DSC curves and X-ray diffraction patterns (Figures 2g and S8), the low-concentration electrolyte (1 m $Zn(OAc)_2$ + 1 m LiCl, LC) exhibits a relatively high solid–liquid transition temperature (−13.6 °C) and forms ice crystals at low temperatures. In contrast, water freezing can be effectively inhibited in the HC electrolyte, thereby achieving a significantly lower freezing point. To understand the antifreezing mechanism from the perspective of the H-bond network in water, an integrated study combining experimental tests with theoretical calculations was conducted. FT-IR spectra reveal that as the LiCl concentration increases, the H—O—H bending vibration undergoes a redshift, and the symmetric O—H stretching mode (~3200 cm^{-1}) weakens, whereas the asymmetric stretching mode (~3400 cm^{-1}) intensifies (Figure 3a). These changes indicate a reduction in H bonds among water molecules and an increase in interactions between ions and water.[47] Raman spectra further corroborate these findings. The broad peaks of O—H stretching vibration, consistent with previous studies,[48,49] can be deconvoluted into three components: strong H bonds in tetrahedral water clusters (~3230 cm^{-1}), weak H bonds involving single or double donors and a single acceptor (~3450 cm^{-1}), and non-H-bonded water (~3630 cm^{-1}). With increasing LiCl concentration, these broad peaks become narrow (Figure 3b), demonstrating weakened strong hydrogen bonding and strengthened weak hydrogen bonding (Figures 3d and S9). This trend suggests that tetrahedral water clusters, which are fundamental to the H-bond network, are disrupted by concentrated salt ions,[47,50,51] and the HC-SiO_2 hydrogel exhibits spectral behavior similar to that of the HC electrolyte. To further elucidate the evolution of H bonds, molecular dynamics (MD) simulations were conducted. As intuitively illustrated in Figure 3c, the number of H-bonds decreases upon the introduction of high-concentration salt ions. Additionally, analyses of radial distribution functions (RDFs) (Figures 3e and S10,11) indicate that the HC and HC-SiO_2 electrolyte enable an increase in ionic hydration, which surpasses hydrogen bonding, leading to the breakdown

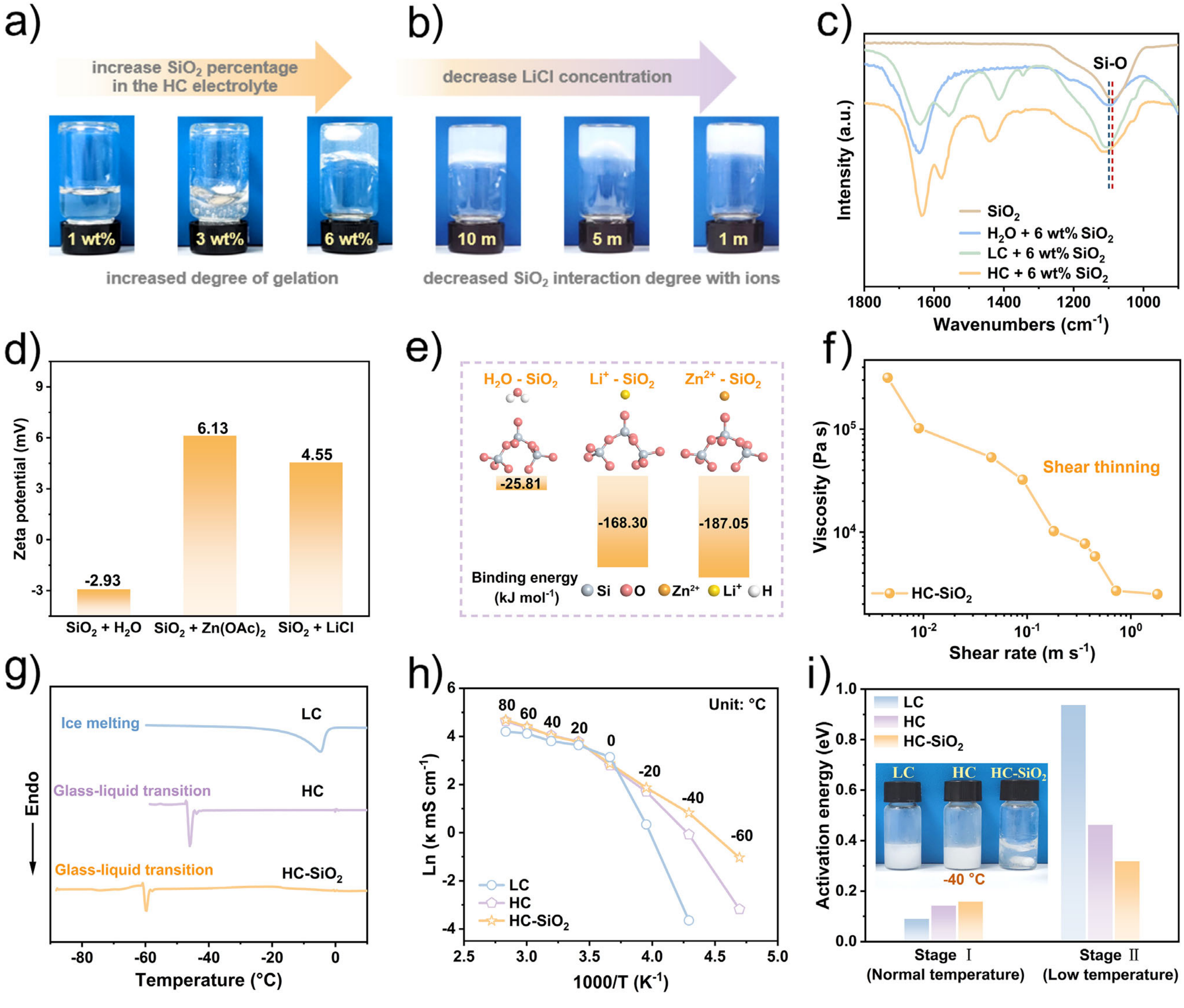

Figure 2. a,b) Photographs: a) HC electrolytes with different SiO_2 mass percentages and b) 1 m $Zn(OAc)_2$ + 6 wt% SiO_2 electrolytes with different LiCl concentrations. c) FT-IR spectra of SiO_2 nanoparticles, H_2O + 6 wt% SiO_2, 1 m $Zn(OAc)_2$ + 1 m LiCl (LC) + 6 wt% SiO_2, and HC-SiO_2 electrolytes. d) Zeta potentials of SiO_2 in pure water, a diluted $Zn(OAc)_2$ solution, and a diluted LiCl solution, respectively. e) Binding energies of water-SiO_2 and cations-SiO_2 obtained by DFT simulations. f) Viscosity as a function of shear rate for the HC-SiO_2 hydrogel. g) Differential scanning calorimeter (DSC) tests of different electrolytes. h) Ionic conductivities of different electrolytes at different temperatures, and i) activation energies calculated from ionic conductivities. The normal-temperature and low-temperature range of the electrolyte were divided by the turning point in the ionic conductivity–temperature curve. The illustration shows different electrolytes at −40 °C.

of tetrahedral water clusters.[38] Consequently, the average number of H bonds per water molecule decreases to below 1.5. These results indicate that the H-bond network in the HC and HC-SiO_2 electrolytes is effectively disrupted by the interactions of concentrated ions with water, thereby suppressing ice nucleation and significantly lowering the freezing point.

Despite the advantages of the concentrated electrolyte, its application is still limited by salt precipitation at low temperatures due to excessively high salt concentrations.[29] However, the introduction of SiO_2 nanoparticles can alleviate this issue by modulating ion behaviors in concentrated electrolytes. As manifested by the fitted Raman peaks of the $[Zn(H_2O)_2Cl_4]^{3-}$ complex[52] and the C–C stretching vibration for OAc$^-$[53] (Figure 3f), high salt concentration causes a blueshift of the peaks, whereas the introduction of SiO_2 mitigates this phenomenon, suggesting that SiO_2 nanoparticles potentially alleviate strong ionic interactions in the HC electrolyte.[54,55] Furthermore, the MD simulations provide quantitative insights into these phenomena. As illustrated in Figures 3h and S12, the HC electrolyte exhibits a significant prevalence of CIPs and AGGs, which increases the system's order and energy, thereby impeding the thermodynamic reduction of the freezing point.[30,31] The Bjerrum's ion-pair formation theory provides a theoretical foundation for understanding this behavior, positing that the close proximity of oppositely charged ions promotes ion associations (Supporting Information). This close interaction between multiple

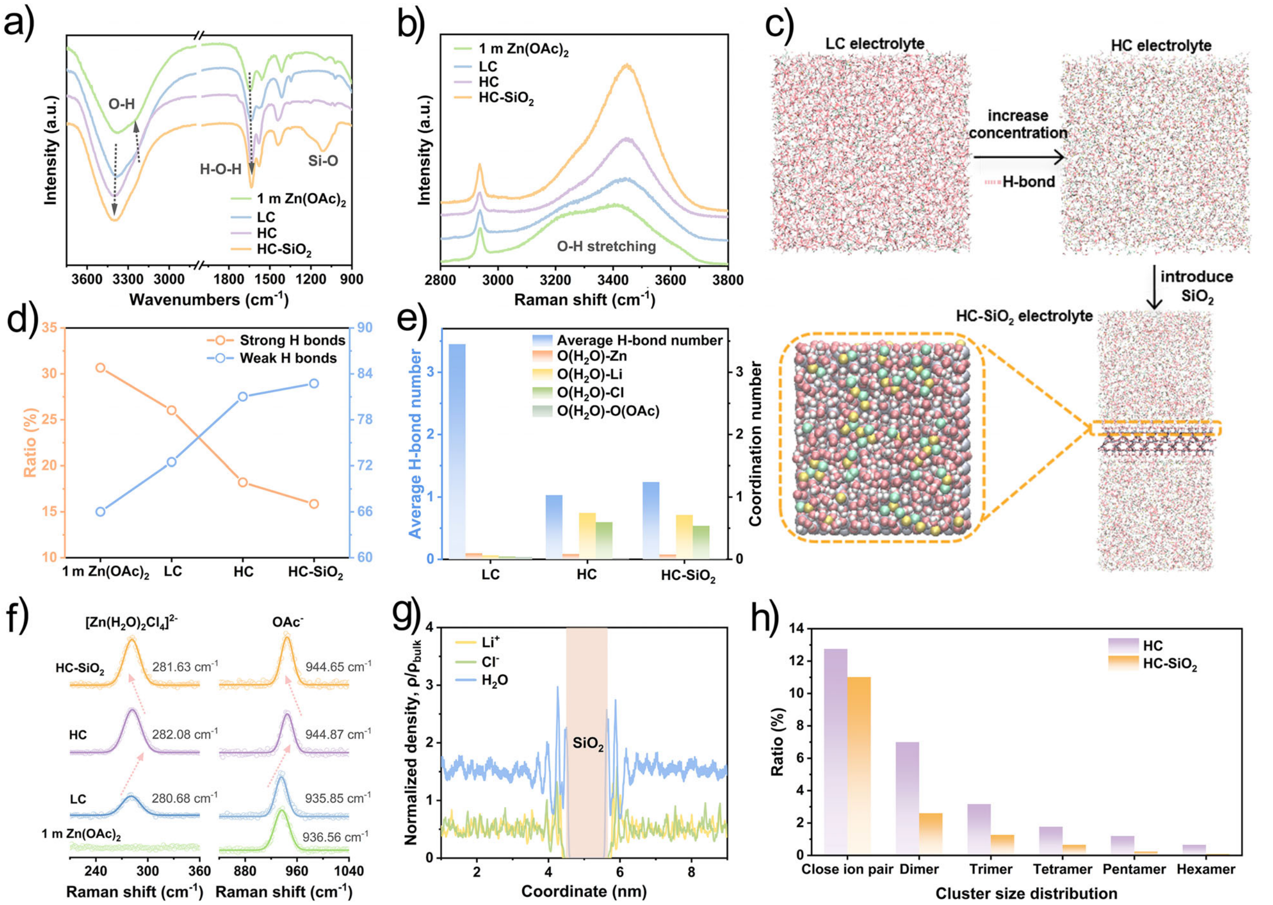

Figure 3. a) FT-IR spectra and b) Raman spectra of different electrolytes. c) MD simulation snapshots of different electrolytes, with H bonds (red dashed lines), hydrogen (off-white), oxygen (red), silicon (grey), Li^+ (yellow), Zn^{2+} (orange), carbon (green), and Cl^- (green). (The enlarged view at the lower left shows water molecules and ions in contact with the SiO_2 slab.) d) Proportions of water with strong H bonds and weak H bonds, determined via fitting the O—H stretching vibration in Raman spectra. e) Average H bond numbers and coordination numbers of water molecules binding to different ions. f) Fitted Raman peaks corresponding to the $[Zn(H_2O)_2Cl_4]^{2-}$ complex and the C—C stretching vibration for OAc^-. g) Density profiles of the HC electrolyte with the SiO_2 slab. The ρ and ρ_{bulk} represent density and bulk density of specified species, respectively. h) Cluster size distributions in the HC and HC-SiO_2 electrolyte.

anions and cations in concentrated electrolytes facilitates the formation of CIPs and continuous AGGs[28,56] Notably, a further reduction in temperature accelerates CIP formation and stabilizes their associations. When attractive forces within CIPs exceeds ionic solvation, these pairs tend to organize into lattice-like ionic arrangements, ultimately resulting in salt precipitation at low temperatures.[57] The presence of SiO_2 nanoparticles introduces molecular-level interactions with water and cations (Figures 3c,3g, and S13), effectively regulating ion-pair distances. As a result, the ratio of CIPs and AGGs significantly decreases from 26.5% (HC system) to 15.8% (HC-SiO_2 system) (Figure 3h). Thermodynamically, the system's order and energy in the concentrated electrolyte can be reduced by the introduction of SiO_2 nanoparticles, leading to the mitigation of the salting-out phenomenon and a further reduction in freezing point. Meanwhile, the improvement in low-temperature ionic conductivity can be attributed to the effect of SiO_2 on reducing the ionic migration energy barrier by weakening ionic interactions in the concentrated electrolyte, which is reflected by a decrease in the activation energy at low temperatures (Figure 2i).

Electrochemical Performance of Zn–I_2 Batteries Operating at Room Temperature

The design of the hydrogel electrolyte is predicted to enable four-electron-transfer iodine cathode, which is firstly confirmed at room temperature. In cathode preparation, I_2 was adsorbed onto adsorption-type active carbon (AC) through the solution-adsorption method.[58] The loading ratio of I_2 to AC was adjusted to maximize I_2 utilization and ensure excellent electrochemical performance (Figure S14). As previously reported,[9,17] nucleophilic Cl^- can stabilize I^+, thereby facilitating the I^+/I_2 couple conversion. As supported by Figures 4a and S15, the LiCl-containing Zn//LC//I_2 full cell exhibits well-defined charge-discharge platforms and redox peaks corresponding to the I^+/I_2 conversion (within 1.5–1.8 V versus Zn^{2+}/Zn), whereas the Zn//I_2 cell with the 1 m $Zn(OAc)_2$ electrolyte fails to exhibit these features. However, the Zn//LC//I_2 cell suffers from overcharging and rapid performance degradation with coulombic efficiencies (CEs) below 80% and a capacity retention below 72.1% after 10 cycles, when tested within the range of 0.6–1.8 V or even

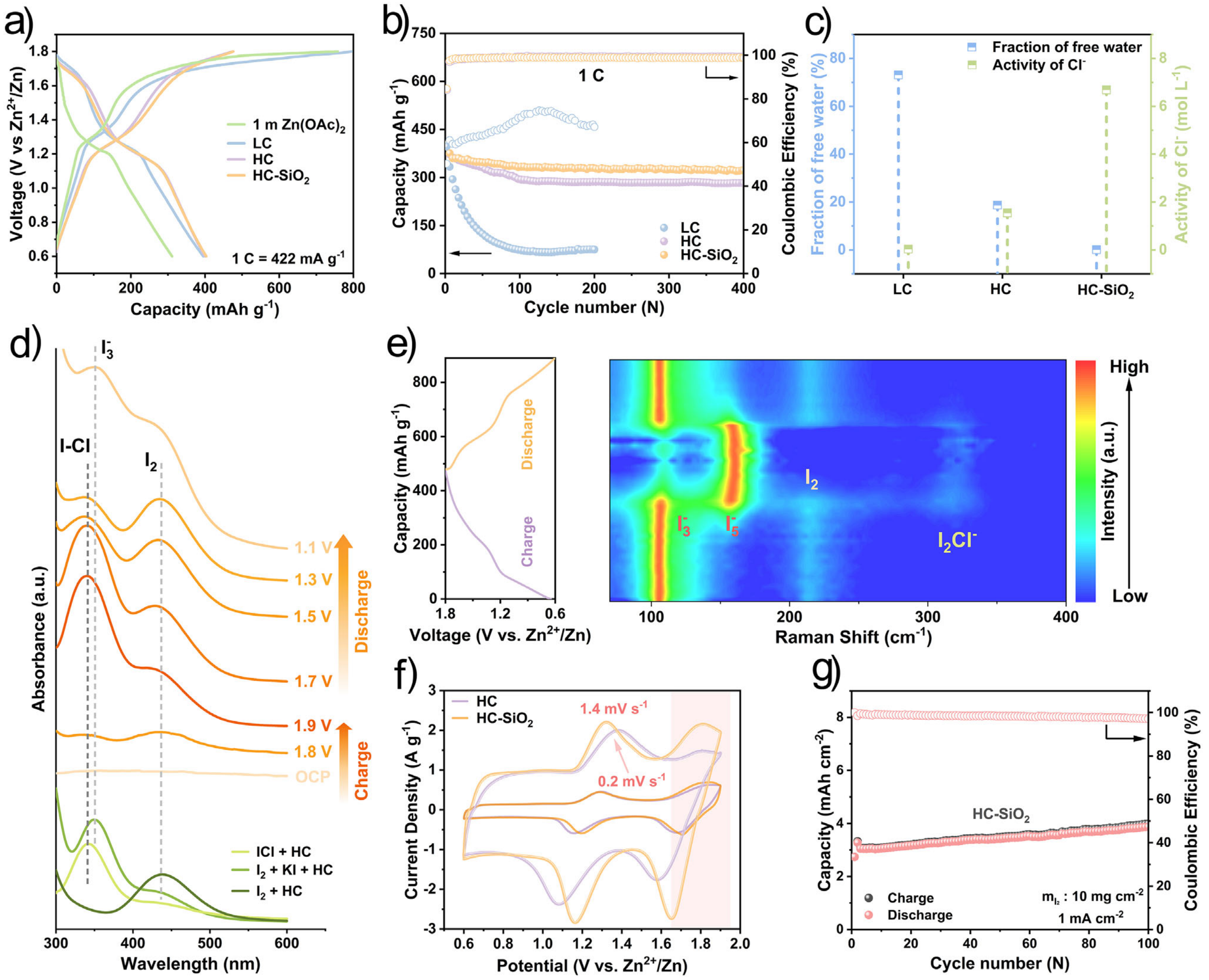

Figure 4. a) First-cycle galvanostatic charge/discharge profiles and b) cycling performance for Zn//I_2 cells in different electrolytes at 1 C. c) Fraction of free water obtained from MD simulations, and the activity of Cl^- calculated by the Nernst equation. d) UV–vis spectra of HC-SiO_2 hydrogel in the Zn//I_2 cell at different charge–discharge stages, compared with UV–vis spectra (green lines) of various commercial iodine species dissolved in the HC electrolyte. e) In situ Raman spectra and corresponding galvanostatic charge–discharge profiles of the Zn//I_2 cell with the HC-SiO_2 hydrogel, tested at 0.5 C. f) CV curves of Zn//I_2 cells in the HC and HC-SiO_2 electrolytes, respectively. g) Cycling performance of Zn//I_2 cell using the HC-SiO_2 hydrogel and about 10 mg cm^{-2} I_2 areal loading, tested at 1 mA cm^{-2}.

1.2–1.8 V (versus Zn^{2+}/Zn) (Figures 4a,b and S16). Besides, Zn//AC cells with the LC electrolyte also display similarly poor performance to the Zn//LC//I_2 cells (Figure S17), indicating substantial water oxidation at elevated charging voltages. These issues can be attributed to the highest free water content (73.1%) in the LC electrolyte, as revealed by MD calculations (Figure 4c). Additionally, elevated water activity accelerates self-discharge in fully charged Zn//I_2 cells with the LC electrolyte (Figure S18a–c) due to I^+ species being readily attacked by water molecules.[17,59] Also, poor interfacial stability between electrodes and the LC electrolyte can accelerate capacity fading during self-discharge testing (Figure S18d–l). In contrast, substantially reduced free water content in HC and HC-SiO_2 electrolytes effectively mitigates water decomposition, contributing to achieving higher CEs exceeding 98.5% at 1 C, and enhancing I^+ stabilization with lower self-discharging rates. Notably, the HC-SiO_2 electrolyte improves the capacity retention of the full cell from 70% (Zn//HC//I_2 cell) to 80% after 400 cycles at 1 C (Figure 4b), which is probably enabled by interfacial modulation of SiO_2 alongside the inherent low-water-activity advantage of concentrated electrolytes. Consequently, constraining water activity is beneficial for enhancing electrochemical stability of four-electron-transfer Zn–I_2 batteries.

To elucidate the four-electron-transfer mechanism of the iodine cathode during the electrochemical charge/discharge process, in situ UV–visible (UV–vis) spectroscopy was conducted (Figures 4d and S19). As charging proceeds to 1.9 V, an absorption peak at around 343 nm emerges, corresponding to the formation of I^+Cl^-. Upon discharging to 1.3 V, the I^+Cl^- peak diminishes, whereas a peak corresponding to I_2 arises at 435 nm, confirming the I^+/I_2 redox reaction. Further discharging results in the appearance of I_3^- at 350 nm, suggesting the I_2/I^- conversion.[60–62] Besides, in situ Raman spectroscopy at the cathode/HC-SiO_2 hydrogel interface (Figures 4e and S20) demonstrates reversible intensity variations of characteristic peaks for I_3^- (106 cm^{-1}), I_5^- (161 cm^{-1}), I_2 (213 cm^{-1}), and I_2Cl^- (~320 cm^{-1}),[62–66] indicating good reversibility of charge storage process using the hydrogel. Ex situ Raman tests on the cathode (Figure S21) complement Raman results by showing a peak of I^+Cl^- (~200 cm^{-1}) at 1.9 V,[63] peaks of I_2Cl^- (300~370 cm^{-1}), I^+Cl^- (with I^0) (~172 cm^{-1}),[62] and I_3^- (~108 cm^{-1}) at 1.6 V, and co-existing I_3^- and I_5^-/ICl^- (~160 cm^{-1}) at 1.1 V, which also reveals the $I^+/I^0/I^-$ pathway in the Zn//HC-SiO_2//I_2 full cell.

Compared to the HC electrolyte, the HC-SiO_2 electrolyte demonstrates significant enhancements in iodine redox kinetics and cycling stability at high rates. Notably, the rate performance test of the Zn//HC-SiO_2//I_2 cell shows improved specific capacities at high rates (Figure S22a). Specifically, for the I^+/I_2 conversion, the Zn//HC-SiO_2//I_2 cell exhibits increased redox peak current in CV curves and decreased charge-transfer impedance (Figures 4f and S23,24), signifying accelerated redox kinetics. These enhancements are attributed to the increased Cl^- activity, which arises from the weakened ionic interactions in the HC-SiO_2 hydrogel (Figures 4c and S25). Besides, the Zn//HC-SiO_2//I_2 cell achieves an extended lifespan during cycling at 5 C (Figure S22b), with 86.7% capacity retention after 3500 cycles. This is likely due to the reduced dissolution of iodine species, facilitated by the high viscosity of the hydrogel and the barrier effect provided by SiO_2 (Figure S26). Importantly, the HC-SiO_2 hydrogel is compatible with high-loading I_2 cathode (~10 mg cm^{-2}), offering a relatively high areal capacity of 3.44 mAh cm^{-2} (Figures 4g and S27), underscoring its practical application potential.

Regarding Zn metal anode compatibility, the HC-SiO_2 hydrogel outperforms the HC and LC electrolytes, enabling a longer lifespan of the Zn//Zn symmetric cell (over 1400 h) and more stable cycling of the Zn//Cu asymmetric cell (over 3600 cycles) with more reversible zinc deposition/stripping behavior (Figures S28, S29). Furthermore, the HC-SiO_2 electrolyte ensures a smoother Zn anode surface after cycling (Figure S30), which benefits from the enhanced 3D diffusion behavior of Zn^{2+} compared to the HC electrolyte (Figure S31). Conversely, the LC electrolyte leads to zinc dendrite growth, caused by the continuous 2D diffusion of Zn^{2+}. From the perspective of ionic coordination environment, the HC-SiO_2 electrolyte minimizes the coordination of water molecules with Zn^{2+} ions (Figure S32), effectively suppressing hydrogen evolution and improving Zn anode compatibility.[67] Besides, potentially owing to decreased ionic interactions caused by SiO_2, the HC-SiO_2 hydrogel can improve Zn^{2+} diffusion and decrease interfacial charge-transfer impedances (R_{ct}) of Zn anode, thereby enhancing anode reaction kinetics (Figures S31 and S33). Consequently, these results validate the effectiveness of the HC-SiO_2 hydrogel in restricting free water and regulating ionic interactions to improve Zn anode reversibility.

Electrochemical Performance of Zn–I_2 Batteries Operating at Low Temperatures

In addition to the antifreezing property, the effectiveness of the cell system utilizing the HC-SiO_2 hydrogel at low temperatures was thoroughly investigated. According to the Arrhenius equation, various reaction kinetics, including the $I^+/I_2/I^-$ conversion, are inherently slowed at low temperatures. However, the suppression of side reactions allows an extended electrochemical stability window of electrolytes (up to 2.0 V versus Zn^{2+}/Zn) (Figure S34). Accordingly, under subzero conditions and at 0.5 C, Zn//I_2 full cells cycling within the 0.6–2.0 V (versus Zn^{2+}/Zn) window achieve CEs over 98%, surpassing those obtained within the 0.6–1.8 V (versus Zn^{2+}/Zn) window at room temperature (below 95%). Also, when Zn//I_2 cells are cycled at 1 C in the 0.6–2.0 V (versus Zn^{2+}/Zn) window at −20 °C, the CEs maintain stability, underscoring the feasibility of this voltage adjustment strategy (Figure S35). Meanwhile, raising the charging cut-off voltage from 1.8 to 2.0 V leads to significant improvements in capacity for the Zn//I_2 cell (Figure S36a–d). To emphasize the necessity of lowering the freezing point, the cycling capacity and corresponding CV curves of Zn//I_2 cells were evaluated using various electrolytes at different temperatures. The LC electrolyte, characterized by a higher freezing point and lower ionic conductivity, enables less than half of the theoretical capacity (122.7 mAh g^{-1}) at −20 °C and virtual failure of the full cell at −40 °C (Figures 5a and S36e,f), as also reflected by significantly decreased current densities in CV curves of the Zn//LC//I_2 cell (Figure S37a). In contrast, at −20 °C, the antifreezing HC-SiO_2 hydrogel supports the complete $I^+/I_2/I^-$ redox peaks and a specific capacity of about 490.9 mAh g^{-1} at 0.5 C (Figures 5b and S38). For practical applications in cold environments, the ability to maintain low-rate cycling stability while achieving high capacities is also an important indicator. Encouragingly, the Zn//HC-SiO_2//I_2 cell can deliver a reversible capacity of over 380 mAh g^{-1} during 200 cycles at 1 C under −20 °C (Figures 5c and S35b). Furthermore, ex situ UV–vis spectroscopy demonstrates that the redox conversions of iodine species at −20 °C are basically consistent with the evolution observed at room temperature, particularly with the emergence of the I^+Cl^- peak (around 335 nm), confirming the existence of the $I^+/I_2/I^-$ conversion at subzero temperatures (Figures 5e and S39).

Due to enhanced ion conduction and increased Cl^- activity, compared to the Zn//HC//I_2 cell, the Zn//HC-SiO_2//I_2 cell can exhibit more conversions of iodine species, especially at temperatures below −20 °C (Figure S37b,c), thereby achieving improved capacities: 372.6 mAh g^{-1} at −40 °C (0.2 C), 363.6 mAh g^{-1} at −50 °C (0.1 C), and 120.1 mAh g^{-1} at −60 °C (0.1 C) (Figures 5a and S36c,d). Furthermore, the Zn//HC-SiO_2//I_2 cell also exhibits superior cycling stability compared to the Zn//HC//I_2 cell. At 5 C and at −20 °C, it delivers an impressive lifespan of 11 000 cycles, maintaining an elevated average capacity of 210 mAh g^{-1} and over 91.7% capacity retention (Figure 5d). At a lower temperature of −40 °C, it also provides average capacities of 200 mAh g^{-1} during 95 cycles at 0.5 C, and 160 mAh g^{-1} during the subsequent 500 cycles at 2 C (Figure S40). Impressively, the

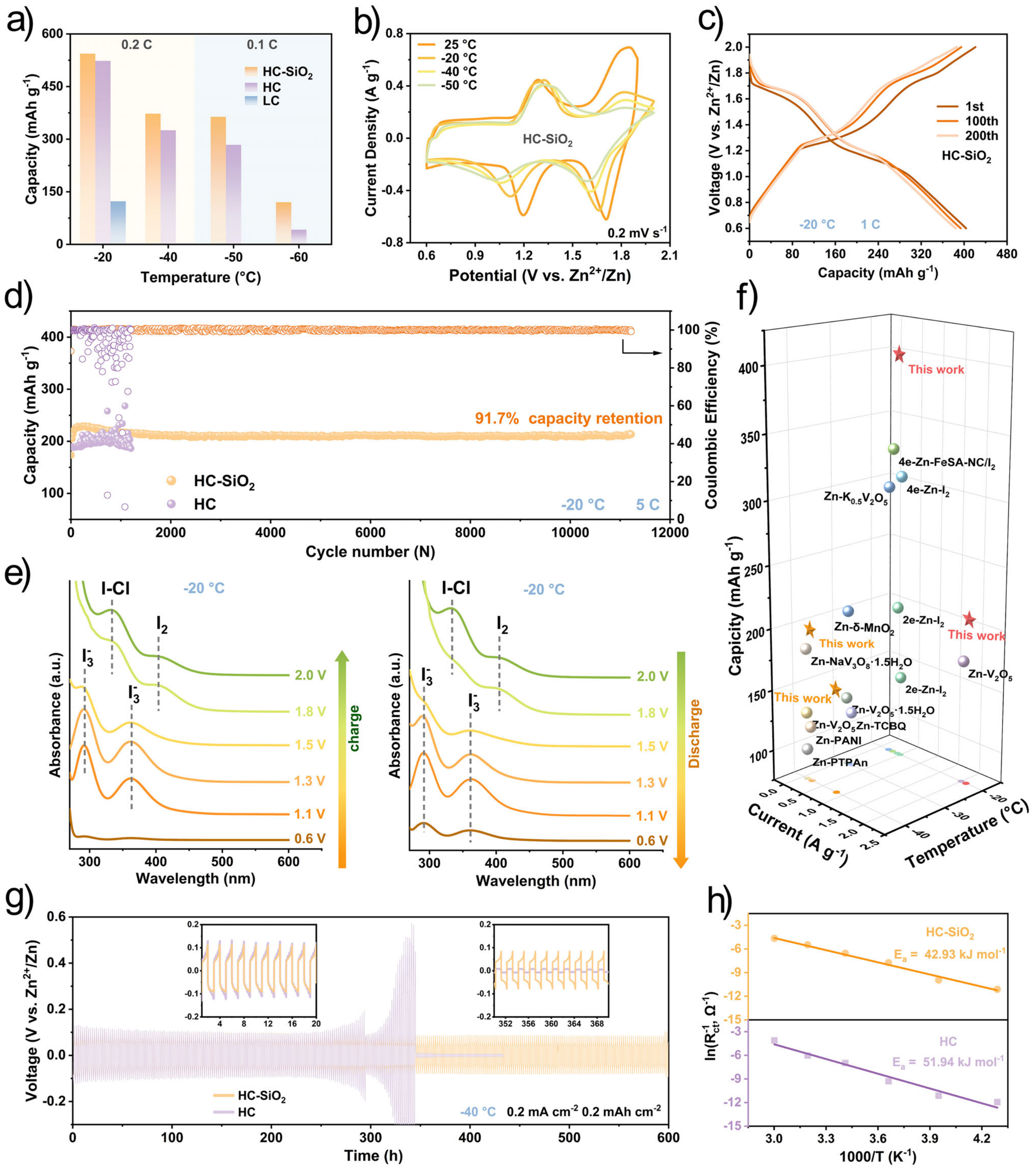

Figure 5. a) Specific capacities of Zn//I$_2$ cells in different electrolytes, tested with 0.2 C (−20, −40 °C) and 0.1 C (−50, −60 °C). b) CV curves of Zn//I$_2$ cells in the HC-SiO$_2$ hydrogel, tested with 0.2 mV s^{-1} at different temperatures. c) Galvanostatic charge–discharge profiles of the Zn//I$_2$ cell in the HC-SiO$_2$ hydrogel, tested with 1 C at −20 °C. d) The cycling performance of Zn//I$_2$ cells in HC and HC-SiO$_2$ electrolytes, tested with 5 C at −20 °C. e) Ex situ UV–vis spectra of iodine species, which were extracted from iodine electrodes at different charge/discharge stages by using acetonitrile. Corresponding full cells were tested with the HC-SiO$_2$ hydrogel at −20 °C. f) Comparison of capacity performance with previously reported low-temperature zinc–metal batteries systems. The traditional two-electron-transfer (I$_2$/I$^-$) Zn–I$_2$ battery is represented as 2e-Zn–I$_2$, whereas the four-electron-transfer (I$^+$/I$_2$/I$^-$) Zn–I$_2$ battery is represented as 4e-Zn–I$_2$. g) The cycling performance of Zn//Zn symmetric cells with the HC and HC-SiO$_2$ electrolytes at −40 °C, tested at 0.2 mA cm^{-2} for 0.2 mAh cm^{-2}. h) Fitted Arrhenius curves and the desolvation energies of Zn^{2+} for the HC and HC-SiO$_2$ electrolytes, calculated from interfacial charge-transfer impedances (R_{ct}) of Zn electrodes.

$Zn//HC\text{-}SiO_2//I_2$ cell outperforms the most recently reported low-temperature zinc–metal battery systems in terms of capacity and cycle life (Figure 5f and Tables S6, S7). Conversely, the $Zn//HC//I_2$ cell exhibits unstable cycling behavior with significantly fluctuating CEs and rapid capacity decay at −40 °C, probably associated with salt precipitation and accumulation at electrode interfaces.[29] Importantly, the $HC\text{-}SiO_2$ hydrogel enables areal capacities of ~2.4 mAh cm^{-2} at −20 °C and ~1.3 mAh cm^{-2} at −40 °C (Figure S41), demonstrating its potential for achieving high areal capacities in low-temperature battery systems.

Similarly, compared to the HC electrolyte, the $HC\text{-}SiO_2$ hydrogel empowers enhanced low-temperature compatibility with Zn metal anode, enabling an extended cycling duration in the Zn//Zn symmetric cell (600 h) and the Zn//Cu asymmetric cell (120 cycles) at −40 °C (Figures 5g and S42). Additionally, it enables lower overpotentials in Zn//Zn cells and improved current density in CV curves of Zn//Cu cells from −40 to −60 °C (Figures S43,44), potentially associated with its lower interfacial charge-transfer impedances and reduced desolvation energy of Zn^{2+} from decreased ionic interactions (Figures 5h and S45). Consequently, the $HC\text{-}SiO_2$ hydrogel also enables respectable anode compatibility.

Conclusion

In summary, we have developed an antifreezing hydrogel electrolyte comprising high-concentration salt and SiO_2 nanoparticles, achieving quasi-solid-state $Zn–I_2$ batteries with the $I^+/I_2/I^-$ redox conversion from room temperature to low temperatures. Unlike conventional hydrogel preparation methods based on water-soluble polymers, sufficient interactions of negatively charged SiO_2 surface with water and cations facilitate the formation of a homogeneous and transparent hydrogel featuring a recoverable "$–SiO_2–$water/ions$–SiO_2–$" network structure, without compromising the ionic conductivity. In addition to preserving the advantageous property of inhibiting ice nucleation resulting from the disrupted H-bond network in the concentrated electrolyte, the $HC\text{-}SiO_2$ hydrogel exhibits reduced CIPs and AGGs due to the interactions of SiO_2 with cations facilitating ion-pair dissociation, further lowering the freezing point from −46.9 °C (HC electrolyte) to −60.7 °C ($HC\text{-}SiO_2$ electrolyte). Beyond achieving stable four-electron-transfer performance at room temperature by suppressing water activity with concentrated salt, the $HC\text{-}SiO_2$ hydrogel facilitates complete $I^+/I_2/I^-$ conversions at low temperatures, as verified by UV–vis spectroscopy, thereby enabling a remarkable capacity of 490.9 mAh g^{-1} at –20 °C. Benefiting from reduced ionic interactions and increased Cl^- activity, the $HC\text{-}SiO_2$ hydrogel enables $Zn//I_2$ cells achieving an average capacity of 210 mAh g^{-1} (5 C) with an impressive lifespan over 11 000 cycles (91.7% retention) at –20 °C, as well as an average capacity of 160 mAh g^{-1} (2 C) without significant degradation during the subsequent 500 cycles at −40 °C, emphasizing the low-temperature application potential of four-electron-transfer $Zn–I_2$ batteries. Accordingly, this study not only provides insights into engineering antifreezing electrolytes grounded in ion-pair formation theory but also offers a promising strategy for the development of low-temperature $Zn–I_2$ batteries based on four-electron-transfer mechanisms.

Acknowledgements

The authors gratefully acknowledge the financial support from the National Natural Science Foundation of China (No. 22379125, 22109030, and 22021001), the Fundamental Research Funds for the Central Universities (20720220073), the Key Research and Development Program of Yunnan Province (202103AA080019), the Fujian Industrial Technology Development and Application Plan (2022I0002). The authors acknowledge Tan Kah Kee Innovation Laboratory for the help with scientific tests. The numerical calculations in this paper have been done on Hefei advanced computing center. The authors acknowledge Prof. Jin-Chao Dong and Dr. Fan Gao from Xiamen University for the assistance with Raman testing.

Conflict of Interests

The authors declare no conflict of interest.

Data Availability Statement

The data that support the findings of this study are available in the Supporting Information of this article.

Keywords: Four-electron redox • Hydrogel • Ionic interaction • Low temperature • $Zn–I_2$ battery

---

[1] B. Dunn, H. Kamath, J.-M. Tarascon, *Science* **2011**, *334*, 928–935.
[2] Z. Zhu, T. Jiang, M. Ali, Y. Meng, Y. Jin, Y. Cui, W. Chen, *Chem. Rev.* **2022**, *122*, 16610–16751.
[3] H. Ahn, D. Kim, M. Lee, K. W. Nam, *Comm. Mater.* **2023**, *4*, 37.
[4] S. Liu, R. Zhang, C. Wang, J. Mao, D. Chao, C. Zhang, S. Zhang, Z. Guo, *Angew. Chem. Int. Ed.* **2024**, *63*, e202400045.
[5] K. K. Turekian, K. H. Wedepohl, *Geol. Soc. Am. Bull.* **1961**, *72*, 175.
[6] H. Chen, X. Li, K. Fang, H. Wang, J. Ning, Y. Hu, *Adv. Energy Mater.* **2023**, *13*, 2302187.
[7] S. Liu, R. Zhang, J. Mao, Y. Zhao, Q. Cai, Z. Guo, *Sci. Adv.* **2022**, *8*, eabn5097.
[8] S.-J. Zhang, J. Hao, H. Wu, C.-C. Kao, Q. Chen, C. Ye, S.-Z. Qiao, *ACS Nano* **2024**, *18*, 28557–28574.
[9] X. Li, M. Li, Z. Huang, G. Liang, Z. Chen, Q. Yang, Q. Huang, C. Zhi, *Energy Environ. Sci.* **2021**, *14*, 407–413.
[10] J. Xu, Z. Huang, H. Zhou, G. He, Y. Zhao, H. Li, *Energy Storage Mater.* **2024**, *72*, 103596.
[11] X. Xie, X. Xu, S. Liang, G. Fang, *J. Energy Chem.* **2025**, *101*, 402–415.
[12] J. Kang, C. Wang, Z. Liu, L. Wang, Y. Meng, Z. Zhai, J. Zhang, H. Lu, *Energy Storage Mater.* **2024**, *68*, 103367.
[13] C. Wang, X. Ji, J. Liang, S. Zhao, X. Zhang, G. Qu, W. Shao, C. Li, G. Zhao, X. Xu, H. Li, *Angew. Chem. Int. Ed.* **2024**, *63*, e202403187.

[14] S. Wang, Y. Wang, Z. Wei, J. Zhu, Z. Chen, H. Hong, Q. Xiong, D. Zhang, S. Li, S. Wang, Y. Huang, C. Zhi, *Adv. Mater.* **2024**, *36*, 2401924.

[15] T. Hu, Y. Zhao, Y. Yang, H. Lv, R. Zhong, F. Ding, F. Mo, H. Hu, C. Zhi, G. Liang, *Adv. Mater.* **2024**, *36*, 2312246.

[16] T. Liu, C. Lei, H. Wang, C. Xu, W. Ma, X. He, X. Liang, *Sci. Bull.* **2024**, *69*, 1674–1685.

[17] Y. Zou, T. Liu, Q. Du, Y. Li, H. Yi, X. Zhou, Z. Li, L. Gao, L. Zhang, X. Liang, *Nat. Commun.* **2021**, *12*, 170.

[18] W. Han, X. Li, *J. Power Sources* **2023**, *580*, 233296.

[19] W. Li, H. Xu, H. Zhang, F. Wei, T. Zhang, Y. Wu, L. Huang, J. Fu, C. Jing, J. Cheng, S. Liu, *Energy Environ. Sci.* **2023**, *16*, 4502–4510.

[20] P. Jiang, Q. Du, C. Lei, C. Xu, T. Liu, X. He, X. Liang, *Chem. Sci.* **2024**, *15*, 3357–3364.

[21] T. Liu, C. Lei, H. Wang, J. Li, P. Jiang, X. He, X. Liang, *Adv. Mater.* **2024**, *36*, 2405473.

[22] T. Liu, C. Lei, H. Wang, W. Yang, X. He, X. Liang, *Chem. Commun.* **2024**, *60*, 7447–7450.

[23] M. Wang, Y. Meng, M. Sajid, Z. Xie, P. Tong, Z. Ma, K. Zhang, D. Shen, R. Luo, L. Song, L. Wu, X. Zheng, X. Li, W. Chen, *Angew. Chem. Int. Ed.* **2024**, *63*, e202404784.

[24] W. Zong, J. Li, C. Zhang, Y. Dai, Y. Ouyang, L. Zhang, J. Li, W. Zhang, R. Chen, H. Dong, X. Gao, J. Zhu, I. P. Parkin, P. R. Shearing, F. Lai, K. Amine, T. Liu, G. He, *J. Am. Chem. Soc.* **2024**, *146*, 21377–21388.

[25] Q. Zhang, Y. Ma, Y. Lu, L. Li, F. Wan, K. Zhang, J. Chen, *Nat. Commun.* **2020**, *11*, 4463.

[26] Y. Zhao, Z. Chen, F. Mo, D. Wang, Y. Guo, Z. Liu, X. Li, Q. Li, G. Liang, C. Zhi, *Adv. Sci.* **2021**, *8*, 2002590.

[27] D. Sheng, X. Liu, Z. Yang, M. Zhang, Y. Li, P. Ren, X. Yan, Z. X. Shen, D. Chao, *Adv. Funct. Mater.* **2024**, *34*, 2402014.

[28] S. Kim, H. Kim, J.-H. Choi, M. Cho, *J. Chem. Phys.* **2014**, *141*, 124510.

[29] S. Han, Q. Guo, H. Mao, Z. Hu, K. Lu, S. Li, Y. Lu, H. Li, X. Huang, L. Chen, Y.-S. Hu, *ACS Energy Lett.* **2024**, *9*, 2276–2285.

[30] J. E. Prue, *J. Chem. Educ.* **1969**, *46*, 12.

[31] K. Goloviznina, A. Serva, M. Salanne, *J. Am. Chem. Soc.* **2024**, *146*, 8142–8148.

[32] C. Zhang, J. Holoubek, X. Wu, A. Daniyar, L. Zhu, C. Chen, D. P. Leonard, I. A. Rodríguez-Pérez, J.-X. Jiang, C. Fang, X. Ji, *Chem. Commun.* **2018**, *54*, 14097–14099.

[33] C. Pfaffenhuber, M. Göbel, J. Popovic, J. Maier, *Phys. Chem. Chem. Phys.* **2013**, *15*, 18318.

[34] P. Ma, Y. Fang, D. Zhang, H. Cheng, N. Fu, X. Zhou, S. Fang, Y. Lin, *ACS Appl. Nano Mater.* **2019**, *3*, 342–350.

[35] Y. F. Zhang, J. M. Dong, C. Tan, S.-k. Huo, J.-y. Wang, Y. He, Y. Y. Wang, *J. Electrochem.* **2021**, *27*, 108–117.

[36] H. Peng, K. Xiao, S. Tian, S. Han, J. Zhou, B. Lu, Z. Chen, J. Zhou, *Adv. Energy Mater.* **2024**, *14*, 2303411.

[37] A. Hu, F. Li, W. Chen, T. Lei, Y. Li, Y. Fan, M. He, F. Wang, M. Zhou, Y. Hu, Y. Yan, B. Chen, J. Zhu, J. Long, X. Wang, J. Xiong, *Adv. Energy Mater.* **2022**, *12*, 2202432.

[38] J. Han, A. Mariani, S. Passerini, A. Varzi, *Energy Environ. Sci.* **2023**, *16*, 1480–1501.

[39] C. Yang, J. Xia, C. Cui, T. P. Pollard, J. Vatamanu, A. Faraone, J. A. Dura, M. Tyagi, A. Kattan, E. Thimsen, J. Xu, W. Song, E. Hu, X. Ji, S. Hou, X. Zhang, M. S. Ding, S. Hwang, D. Su, Y. Ren, X.-Q. Yang, H. Wang, O. Borodin, C. Wang, *Nat. Sust.* **2023**, *6*, 325–335.

[40] X. Zeng, B. Zeng, L. Huang, L. Zhong, X. Li, W. Huang, *Minerals* **2022**, *12*, 1128.

[41] L.-l. Zhi, G.-f. Zhao, L.-j. Guo, Q. Jing, *Phys. Rev. B* **2008**, *77*, 235435.

[42] S. Wang, L. Yu, S. Wang, L. Zhang, L. Chen, X. Xu, Z. Song, H. Liu, C. Chen, *Nat. Commun.* **2022**, *13*, 3408.

[43] C. Pfaffenhuber, F. Hoffmann, M. Fröba, J. Popovic, J. Maier, *J. Mater. Chem. A* **2013**, *1*, 12560.

[44] M. Matsumoto, S. Saito, I. Ohmine, *Nature* **2002**, *416*, 409–413.

[45] J. D. Smith, C. D. Cappa, K. R. Wilson, R. C. Cohen, P. L. Geissler, R. J. Saykally, *Proc. Natl. Acad. Sci. USA* **2005**, *102*, 14171–14174.

[46] T. D. Kühne, R. Z. Khaliullin, *J. Am. Chem. Soc.* **2014**, *136*, 3395–3399.

[47] J. Zheng, G. Tan, P. Shan, T. Liu, J. Hu, Y. Feng, L. Yang, M. Zhang, Z. Chen, Y. Lin, J. Lu, J. C. Neuefeind, Y. Ren, K. Amine, L.-W. Wang, K. Xu, F. Pan, *Chem* **2018**, *4*, 2872–2882.

[48] Y. Tominaga, A. Fujiwara, Y. Amo, *Fluid Phase Equilib.* **1998**, *144*, 323–330.

[49] M. Turgeman, V. Wineman-Fisher, F. Malchik, A. Saha, G. Bergman, B. Gavriel, T. R. Penki, A. Nimkar, V. Baranauskaite, H. Aviv, M. D. Levi, M. Noked, D. T. Major, N. Shpigel, D. Aurbach, *Cell Rep. Phys. Sci.* **2022**, *3*, 100688.

[50] Y. Gao, H. Fang, K. Ni, Y. Feng, *Sci. Rep.* **2022**, *12*, 8036.

[51] F. Tanga, Z. Lib, C. Zhanga, S. G. Louieb, R. Card, D. Y. Qiue, X. Wua, *Proc. Natl. Acad. Sci. USA* **2022**, *119*, e2201258119.

[52] D. E. Irish, B. McCarroll, T. F. Young, *J. Chem. Phys.* **1963**, *39*, 3436–3444.

[53] M. S. Ghazvini, G. Pulletikurthi, A. Lahiri, F. Endres, *ChemElectroChem* **2016**, *3*, 598–604.

[54] R. L. Fros, D. W. Jame, *J. Chem. Soc. Faraday Trans. I* **1982**, *78*, 3223–3234.

[55] J.-Y. Yu, Y. Zhang, S.-H. Tan, Y. Liu, Y.-H. Zhang, *J. Phys. Chem. B* **2012**, *116*, 12581–12589.

[56] M. B. Singh, V. H. Dalvi, V. G. Gaikar, *RSC Adv.* **2015**, *5*, 15328–15337.

[57] D. Reber, R.-S. Kühnel, C. Battaglia, *ACS Mater. Lett.* **2019**, *1*, 44–51.

[58] Q. Zhao, Y. Lu, Z. Zhu, Z. Tao, J. Chen, *Nano Lett.* **2015**, *15*, 5982–5987.

[59] Y. L. Wang, J. C. Nagy, D. W. Margerum, *J. Am. Chem. Soc.* **1989**, *111*, 7838–7844.

[60] A. E. Gillam, R. A. Morton, *Proc. R. Soc. A: Math. Phys. Eng. Sci.* **1931**, *132*, 152–167.

[61] D. J. Seery, D. Britton, *J. Phys. Chem.* **1964**, *68*, 2263–2266.

[62] S. Schott, L. Ress, J. Hrušák, P. Nuernberger, T. Brixner, *Phys. Chem. Chem. Phys.* **2016**, *18*, 33287–33302.

[63] P. Klaboe, *J. Am. Chem. Soc.* **1967**, *89*, 3667–3676.

[64] P. Deplano, J. R. Ferraro, M. L. Mercuri, E. F. Trogu, *Coord. Chem. Rev.* **1999**, *188*, 71–95.

[65] R. L. Remmele, P. F. McMillan, *Spectrosc. Lett.* **1987**, *20*, 757–762.

[66] L. Alvarez, J. L. Bantignies, R. Le Parc, R. Aznar, J. L. Sauvajol, A. Merlen, D. Machon, A. San Miguel, *Phys. Rev. B* **2010**, *82*, 205403.

[67] S. Chen, D. Ji, Q. Chen, J. Ma, S. Hou, J. Zhang, *Nat. Commun.* **2023**, *14*, 3526.

Manuscript received: January 23, 2025
Revised manuscript received: March 14, 2025
Accepted manuscript online: March 14, 2025
Version of record online: ■■, ■■

Forschungsartikel

Zn–I_2 Batteries

M. Chen, G. Chen, C. Sun, X. Li, M. Zhang, H. Hua, J. Zhao*, Y. Yang* — **e202502005**

SiO_2 Nanoparticles-Induced Antifreezing Hydrogel Electrolyte Enables Zn–I_2 Batteries with Complete and Reversible Four-Electron-Transfer Mechanisms at Low Temperatures

An antifreezing hydrogel electrolyte (HC-SiO_2) is developed through the gelation of a high-concentration electrolyte (1 m $Zn(OAc)_2$ + 21 m LiCl, HC) with SiO_2 nanoparticles. The interactions between negatively charged SiO_2 surface and cations facilitate a reduction in close ion-pairs (CIPs) and aggregations (AGGs) by dissociating ion-pairs, which alleviates salt precipitation in the concentrated electrolyte and further lowers the freezing point, enabling low-temperature operation of quasi-solid-state Zn–I_2 batteries with complete and reversible $I^-/I_2/I^+Cl^-$ processes.